Modelling the suppression of viscous fingering in elastic-walled Hele-Shaw cells

DRAGA PIHLER-PUZOVIĆ†, RAPHAËL PÉRILLAT, MATTHEW RUSSELL, ANNE JUEL AND MATTHIAS HEIL

Manchester Centre for Nonlinear Dynamics and School of Mathematics, University of Manchester, Oxford Road, Manchester, M13 9PL, UK

Recent experiments by Pihler-Puzović *et al.* (2012) have shown that the onset of viscous fingering in circular Hele-Shaw cells in which an air bubble displaces a viscous fluid is delayed considerably when the top boundary of the cell is replaced by an elastic membrane. Non-axisymmetric instabilities are only observed at much larger flow rates, and the large-amplitude fingers that develop are fundamentally different from the dendritic fingers in rigid-walled cells.

We explain the mechanism for the suppression of the instability using a combination of linear stability analysis and direct numerical simulations, based on a theoretical model that couples a depth-averaged lubrication equation for the fluid flow to the Föppl-von Kármán equations, which describe the deformation of the elastic membrane. We show that fluid-structure interaction affects the instability primarily via two changes to the axisymmetric base flow: the axisymmetric inflation of the membrane prior to the onset of any instabilities slows down the expansion of the air bubble and forces the air-liquid interface to propagate into a converging fluid-filled gap. Both of these changes reduce the destabilising viscous effects that drive the fingering instability in a rigid-walled cell. In contrast, capillary effects only play a very minor role in the suppression of the instability.

1. Introduction

The development of viscous fingers in Hele-Shaw cells is a classical and widely studied fluid mechanical instability. When air is injected into a viscous fluid layer that fills the narrow gap between two rigid, parallel plates, the radially expanding air bubble that displaces the viscous fluid tends to be unstable to non-axisymmetric perturbations. These perturbations grow rapidly into large-amplitude fingers, which undergo repeated tip-splitting, resulting in complex dendritic structures such as the one shown in Fig. 1 (a); see, *e. g.*, Saffman & Taylor (1958); Paterson (1981); Homsy (1987); Thomé *et al.* (1989); Chen (1989); Miranda & Widom (1998).

The continuing interest in viscous fingering arises from its close relation to a wide range of phenomena, such as the printer's and ribbing instabilities (Taylor 1963; McEwan & Taylor 1966; Reinelt 1995), the solidification instability in crystal growth (Mullins & Sekerka 1964), the dynamics of fractures (Hull 1999), the Darrieus-Landau instability of flame fronts (Clanet & Searby 1998) and growth of bacterial colonies (Ben Jacob *et al.* 1992). Moreover, it is of direct practical relevance in fields like oil recovery (Orr Jr. & Taber 1984) and carbon sequestration (Cinar *et al.* 2009). Much recent work has focused on mechanisms that can be used to manipulate the pattern formation in Hele-Shaw cells, *e. g.* via the use of non-Newtonian fluids (Kondic *et al.* 1998; Fast *et al.* 2001), by

† Email address for correspondence: draga.pihler-puzovic@manchester.ac.uk

(a) Dendritic fingers:
$\dot{V} = 145$ ml.min^{-1}

(b) Suppressed fingers:
$\dot{V} = 145$ ml.min^{-1}

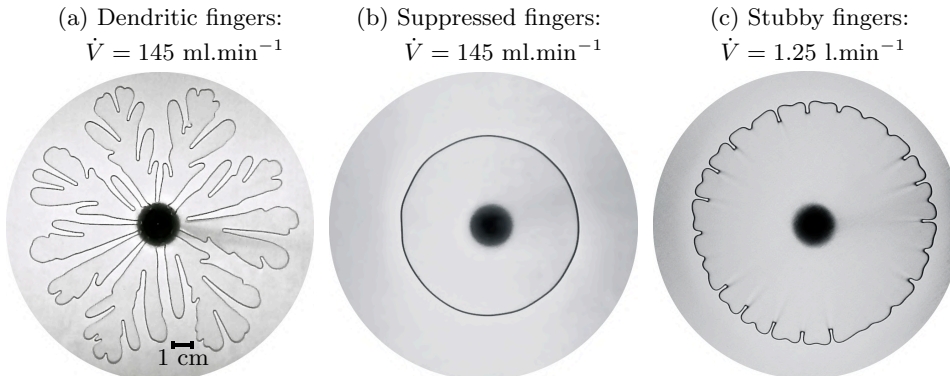(c) Stubby fingers:
$\dot{V} = 1.25$ l.min^{-1}

1 cm

FIGURE 1. Top view of the fingering patterns in (a) the rigid cell and (b, c) the elastic-walled cell with a latex membrane of thickness $h \approx 0.33$ mm and Young's modulus $E = 1.44$ MPa, in which a growing air bubble displaces silicone oil of viscosity $\mu = 1.04$ kg m^{-1}s^{-1} at a constant flow rate $\dot{V}$.

controlling the injection rate (Li *et al.* 2009; Dias & Miranda 2010; Dias *et al.* 2012) or by changing the geometry of the cell (Al Housseiny *et al.* 2012; Juel 2012).

In recent experimental work (Pihler-Puzović *et al.* 2012) we showed that the introduction of fluid-structure interaction is a particularly powerful means of affecting the viscous fingering instability. Specifically, we found that when the upper bounding plate of the Hele-Shaw cell was replaced by an elastic membrane, the onset of fingering was delayed considerably: for an injection flow rate that created the complex dendritic fingering pattern shown in Fig. 1 (a), the expanding bubble remained axisymmetric in an (otherwise identical) elastic-walled cell; see Fig. 1 (b). Non-axisymmetric instabilities still developed, but only at much larger flow rates. Furthermore, the finite-amplitude fingers that ultimately emerged from instabilities in the elastic-walled cell were found to have a fundamentally different shape ("short and stubby"; see Fig. 1 (c)) compared to the narrow dendritic fingers in rigid-walled cells.

Similar interactions between compliant boundaries and lubrication flows also arise in a variety of natural processes including pulmonary airways reopening (Jensen *et al.* 2002; Grotberg & Jensen 2004; Heap & Juel 2008; Heil & Hazel 2011) and the spreading of magma underneath deforming strata (Michaut 2011; Bunger & Cruden 2011; Lister *et al.* 2013), as well as industrial application, such as roll coating (Carvalho & Scriven 1997, 1999; Chong *et al.* 2007) and fabrication of MEMS (Hosoi & Mahadevan 2004).

The aim of the present paper is to develop a theoretical model of flow in elastic-walled Hele-Shaw cells in order to elucidate the mechanism responsible for the suppression of viscous fingering by fluid-structure interaction. Our model is based on the classical work by Saffman & Taylor (1958), who developed a two-dimensional viscous potential flow model for the depth-averaged velocities in rigid-walled Hele-Shaw cells. In §2 we extend this model by coupling it to the Föppl-von Kármán equations which describe the wall deformation, accounting for both stretching and bending of the bounding membrane. §3 provides an overview of the methods used for the analysis – a linear stability analysis, complemented by direct numerical simulations of the full nonlinear equations. In §4 we analyse the system's behaviour, studying the effect of fluid-structure interaction on the axisymmetric base flow, its (linear) stability to non-axisymmetric perturbations, and the evolution of the finite-amplitude fingers that develop from the initial instability. Throughout this paper, we vary the the importance of fluid-structure interaction via
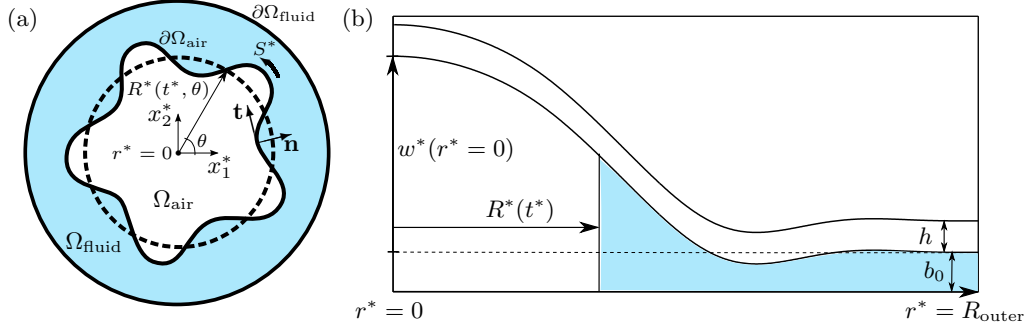
FIGURE 2. Diagram of the elastic Hele-Shaw cell: (a) top view, (b) radial cross-section. All quantities are given in dimensional variables. Shaded domains indicate the regions occupied by the viscous fluid.

changes to the stiffness of the elastic membrane. This allows us to identify the mechanism responsible for the suppression of viscous fingering in elastic-walled Hele-Shaw cells, which we explain in §5. Finally, in §6 we provide a brief discussion and our conclusions.

2. The model

2.1. *Flow equations*

A sketch of the problem setup is shown in Fig. 2: a circular Hele-Shaw cell of radius R_{outer} whose upper boundary is formed by an elastic membrane of thickness h, Young's modulus E and Poisson's ratio ν. When the membrane is in its undeformed configuration, the cell has a uniform depth $b_0 \ll R_{\text{outer}}$. Air is injected at a constant flow rate $\dot{V}$ at the centre of the cell (at $r = 0$) and displaces the viscous fluid (of viscosity μ and surface tension γ) that occupies the region Ω_{fluid}. We non-dimensionalise all lengths in the plane of the cell on the outer radius, $[x_1^*, x_2^*, r^*] = [x_1, x_2, r]\, R_{\text{outer}}$, and time on the natural time scale for flux-driven flow in the narrow gap between the walls of the cell, $t^* = \mathcal{T}t$, where $\mathcal{T} = 2\pi R_{\text{outer}}{}^2 b_0 / \dot{V}$. Throughout this paper a superscript asterisk is used to distinguish dimensional quantities from their non-dimensional equivalents. Given the small aspect ratio of the cell, $\mathcal{A} = b_0 / R_{\text{outer}} \ll 1$, we describe the flow of the viscous fluid by the Reynolds lubrication equation (Reynolds 1886),

$$\frac{\partial b}{\partial t} = \nabla \cdot \left(b^3 \nabla p \right) \quad \text{in} \quad \Omega_{\text{fluid}}, \tag{2.1}$$

where $b = b^*/b_0$ is the non-dimensional depth of the Hele-Shaw cell (which depends on the deformation of the elastic membrane) and $p = p^*/(6\mu\dot{V}/(\pi b_0{}^3))$ is the non-dimensional fluid pressure.

Mass conservation for the volume of air in the bubble region, Ω_{air}, requires that

$$\int_{\Omega_{\text{air}}(t)} b(x_1, x_2, t)\, dx_1 dx_2 = \int_{\Omega_{\text{air}}(t=0)} b(x_1, x_2, t=0)\, dx_1 dx_2 + 2\pi t. \tag{2.2}$$

We describe the position of the air-liquid interface by the vector $\mathbf{R} = \mathbf{R}^*/R_{\text{outer}} = R(\theta, t)\, \mathbf{e}_r$ (see Fig. 2). Its evolution is governed by the kinematic boundary condition

$$\frac{\partial \mathbf{R}}{\partial t} \cdot \mathbf{n} = \mathbf{u} \cdot \mathbf{n} \quad \text{at} \quad \partial\Omega_{\text{air}}, \tag{2.3}$$

where $\mathbf{n}$ is the unit normal to the air-liquid interface pointing into the viscous fluid and

$$\mathbf{u} = -b^2 \nabla p \tag{2.4}$$

is the non-dimensional depth-averaged fluid velocity. We assume the pressure at the outer edge of the Hele-Shaw cell to be atmospheric and set

$$p(r = 1) = 0. \tag{2.5}$$

The capillary pressure jump over the curved air-liquid interface requires that

$$p|_{\partial\Omega_{\text{air}}} = p_{\text{B}}(t) - \frac{1}{12}Ca^{-1}\,\mathcal{A}\,\kappa_{\text{mean}} \tag{2.6}$$

where $Ca = \mu R_{\text{outer}}/\gamma\mathcal{T}$ is the capillary number and $p_B(t)$ is the non-dimensional bubble pressure, assumed to be spatially constant. $\kappa_{\text{mean}} = R_{\text{outer}}\kappa^*_{\text{mean}}$ is the non-dimensional mean curvature of the air-liquid interface, which we approximate by the sum of the in-plane and transverse interface curvatures as

$$\kappa_{\text{mean}} = \kappa_{\parallel} + \kappa_{\perp} = \mathcal{A}\frac{\partial \mathbf{t}}{\partial S} \cdot \mathbf{n} + \frac{2}{b}, \tag{2.7}$$

where $\mathbf{t}$ is the unit tangent to the air-liquid interface (in the plane of the Hele-Shaw cell) pointing in the direction of an increase in the arclength $S = S^*/R_{\text{outer}}$; see Fig. 2 (a). The expression for the transverse curvature, $\kappa_{\perp} = 2/b$, is itself an approximation (see Fig. 7 below for a sketch of the assumed interface geometry).

We note that, as in the classical theory of Saffman & Taylor (1958), our dynamic boundary condition (2.6) neglects the viscous normal stresses at the air-liquid interface. Furthermore, the kinematic boundary condition (2.3) ignores the fact that a thin layer of viscous fluid is deposited on the bounding plates of the Hele-Shaw cell. Both effects could, in principle, be incorporated into the model using approaches similar to those of Reinelt (1987), Jensen *et al.* (2002), Gadêlha & Miranda (2009) or Kim *et al.* (2009).

2.2. *Membrane equations*

In the experiments by Pihler-Puzović *et al.* (2012) the vertical deflection of the membrane, $w^* = wR_{\text{outer}}$, in response to the fluid pressure tended to be large compared to the membrane's thickness. This suggests that self-induced in-plane stresses make an important contribution to the membrane's elastic response. We therefore describe the deformation of the membrane by the non-dimensional Föppl-von Kármán equations (Landau & Lifshitz 1970):

$$\nabla^4 w - \eta \left[\frac{\partial^2 \phi}{\partial x_2^2} \frac{\partial^2 w}{\partial x_1^2} + \frac{\partial^2 \phi}{\partial x_1^2} \frac{\partial^2 w}{\partial x_2^2} - 2 \frac{\partial^2 \phi}{\partial x_1 \partial x_2} \frac{\partial^2 w}{\partial x_1 \partial x_2} \right] = P, \tag{2.8}$$

$$\nabla^4 \phi + \left[\frac{\partial^2 w}{\partial x_1^2} \frac{\partial^2 w}{\partial x_2^2} - \left(\frac{\partial^2 w}{\partial x_1 \partial x_2} \right)^2 \right] = 0, \tag{2.9}$$

where we scaled the pressure acting on the membrane using the bending modulus $K = Eh^3/12(1 - \nu^2)$ so that $P = P^* R_{\text{outer}}^3/K$. The function $\phi = \phi^*/(EhR_{\text{outer}})$ is an Airy stress function for the in-plane stresses in the membrane (such that $\sigma_{11} = \partial^2\phi/\partial x_2^2$, $\sigma_{22} = \partial^2\phi/\partial x_1^2$ and $\sigma_{12} = -\partial^2\phi/\partial x_1\partial x_2$), non-dimensionalised on the Young's modulus of the membrane. Finally, $\eta = 12(1 - \nu^2)\left(R_{\text{outer}}/h\right)^2$ is a parameter that controls the relative importance of in-plane and bending stresses. For sufficiently small deflections, $|w^*| \ll h$, the nonlinear terms in the Föppl-von Kármán equations can be neglected and the transverse deflections are governed by the classical linear bending equation $\nabla^4 w = P$.

In the experiments the membrane rested freely on the viscous fluid layer and no significant deformation was observed far ahead of the air-liquid interface. We mimic this behaviour by assuming the membrane to be clamped and free of any in-plane stresses at

its outer boundary by setting

$$w = 0, \quad \frac{\partial w}{\partial n} = 0, \quad \phi = 0, \quad \frac{\partial \phi}{\partial n} = 0 \quad \text{at } r = 1. \tag{2.10}$$

2.3. *The coupled problem*

The fluid and solid equations are coupled because the pressure in the Föppl-von Kármán equation (2.8) depends on the pressure in the fluid and the bubble

$$P = \begin{cases} \mathcal{I} \, p_B & \text{in } \Omega_{\text{air}}, \\ \mathcal{I} \, p & \text{in } \Omega_{\text{fluid}}, \end{cases} \tag{2.11}$$

where the final non-dimensional parameter, $\mathcal{I} = 12\mu\dot{V}/2\pi\mathcal{A}^3 K$, provides a measure of the typical viscous stresses in the fluid relative to the stiffness of the elastic membrane. The parameter $\mathcal{I}$ gives an indication of the importance of fluid-structure interaction (FSI) in the sense that as $\mathcal{I} \to 0$ the membrane no longer "feels" the fluid stresses and the system's behaviour approaches that of a rigid-walled Hele-Shaw cell.

Furthermore, the membrane deflection affects the depth of the Hele-Shaw cell in (2.1), (2.2), (2.3) and (2.7) via

$$b = 1 + w/\mathcal{A}. \tag{2.12}$$

3. Solution

We study the system's behaviour using two complementary approaches. We perform a linear stability analysis to assess the growth (or decay) of small-amplitude non-axisymmetric perturbations to an axisymmetrically growing bubble and then use direct numerical simulations of the full nonlinear equations to study the evolution of the instabilities in the large-amplitude regime.

3.1. *Linear stability analysis*

To determine the system's axisymmetric evolution we expressed the governing equations in cylindrical polar coordinates and assumed $p = \bar{p}(r,t)$, $w = \bar{w}(r,t)$, $\phi = \bar{\phi}(r,t)$ and $R = \bar{R}(t)$. This transforms equations (2.1)-(2.12) into a spatially one-dimensional system of PDEs with a free boundary, listed in Appendix B. We employed the time-dependent transformations

$$\xi_1 = \frac{r}{\bar{R}(t)} \qquad \text{for } r \in [0, \bar{R}(t)], \quad \text{and} \quad \xi_2 = \frac{r - \bar{R}(t)}{1 - \bar{R}(t)} \qquad \text{for } r \in [\bar{R}(t), 1] \tag{3.1}$$

to map the moving domain into two fixed reference domains and discretised the spatial derivatives with respect to ξ_1 and ξ_2 by second-order accurate central finite-differences, using virtual points for the boundary conditions. Starting from the initial condition $\bar{w}(r, t = 0) = 0$ and $\bar{R}(t = 0) = R_{\text{init}}$ we then employed the first-order BDF scheme to evolve the solution.

To assess the stability of the evolving axisymmetric solution to non-axisymmetric perturbations we substituted the ansatz $p = \bar{p}(r,t) + \varepsilon\hat{p}(r,t)\cos(N\theta)$, $w = \bar{w}(r,t) + \varepsilon\hat{w}(r,t)\cos(N\theta)$, $\phi = \bar{\phi}(r,t) + \varepsilon\hat{\phi}(r,t)\cos(N\theta)$, $R = \bar{R}(t) + \varepsilon\hat{R}(t)\cos(N\theta)$ into the equations and linearised with respect to the amplitude $\varepsilon \ll 1$. This yields another spatially one-dimensional system of PDEs for the evolution of the perturbations $[\hat{p}(r,t), \hat{w}(r,t), \hat{\phi}(r,t), \hat{R}(t)]$ with a given azimuthal wavenumber N (see Appendix B). The system of PDEs is linear in the perturbation quantities but has time-dependent coefficients that arise from the time-dependence of the evolving axisymmetric base state. We discretised

the equations by the same finite-difference scheme that we employed for the axisymmetric equations and followed the growth or decay of the perturbations by time-stepping the equations, starting from a non-zero initial condition for $\hat{R}(t=0)$.

3.2. *Direct numerical simulations*

We performed direct numerical simulations using the object-oriented multi-physics finite-element library `oomph-lib` (Heil & Hazel 2006). The full nonlinear system of PDEs (2.1)-(2.12) was discretised on an unstructured moving mesh, generated with the open-source mesh generator `Triangle` (Shewchuk 1996). The initial mesh was designed so that the air-liquid interface was aligned with an internal mesh boundary. To ensure that this line followed the motion of the air-liquid interface, we treated the mesh as a (pseudo-)elastic solid body which we deformed by applying a suitable line traction, $\mathfrak{p}\,\mathbf{n}$, along the air-liquid interface.

In the region Ω_{fluid} the fluid pressure was expressed as $p = \sum_j P_j\,\psi_j$, where ψ_j are the piecewise-quadratic shape functions associated with the six-noded triangles that make up the mesh. Using the basis functions as the test functions, we integrated the Galerkin weak form of the equation (2.1) by parts to obtain the discrete residuals

$$r_j^{[p]} = \int_{\Omega_{\text{fluid}}} \left(b^3 \frac{\partial p}{\partial x_k} \frac{\partial \psi_j}{\partial x_k} + \frac{\partial b}{\partial t} \psi_j \right) dx_1 dx_2 + \oint_{\partial\Omega_{\text{air}}} b \frac{\partial \mathbf{R}}{\partial t} \cdot \mathbf{n}\,\widetilde{\psi_j}\,dS = 0 \qquad (3.2)$$

which we treated as the equations for the unknown nodal pressures, P_j. Note that in (3.2) the kinematic boundary condition (2.3) and the relation (2.4) were used to replace the normal derivative of the pressure in the boundary integral by the instantaneous normal velocity of the air-liquid interface. Throughout this section a tilde indicates that a shape function is to be evaluated along the line representing the air-liquid interface. The subscript j enumerates discrete unknowns and the associated residual equations. Other subscripts take values 1 and 2, indicating the coordinate directions, and the summation convention is used for these.

The weak form of the dynamic boundary condition (2.6),

$$r_j^{[\mathfrak{p}]} = \oint_{\partial\Omega_{\text{air}}} \left[p - p_{\text{B}}(t) + \frac{1}{12} Ca^{-1}\,\mathcal{A}\left(\mathcal{A}\,\boldsymbol{\tau} \cdot \mathbf{n} + \frac{2}{b} \right) \right] \widetilde{\psi_j}\,dS = 0, \qquad (3.3)$$

was then used as the equation for the nodal values $\mathfrak{P}_j$ of the line traction (expanded as $\mathfrak{p} = \sum_j \mathfrak{P}_j\,\widetilde{\psi_j}$), which drives the deformation of the pseudo-solid mesh in response to the motion of the air-liquid interface. In (3.3) we have replaced the derivative of the tangent vector, $\partial \mathbf{t}/\partial S$, by its smoothed counterpart, $\boldsymbol{\tau}$. We expanded its Cartesian components, τ_i, as $\tau_i = \sum_j T_{ij}\,\widetilde{\psi_j}$, and determined the coefficients, T_{ij}, from the integrated-by-parts projection equation

$$r_{ij}^{[\tau]} = \oint_{\partial\Omega_{\text{air}}} \left(\tau_i \widetilde{\psi_j} + t_i \frac{\partial \widetilde{\psi_j}}{\partial S} \right) dS = 0. \qquad (3.4)$$

This projection is required because, given the piecewise quadratic representation of the air-liquid interface in the moving mesh, $\partial \mathbf{t}/\partial S$ is not sufficiently smooth to allow a direct evaluation of the line integral in equation (3.3). Finally, we used the discretised version of the volume constraint (2.2) as the equation that determines the bubble pressure $p_{\text{B}}(t)$.

To discretise the biharmonic operators in (2.8) and (2.9) we employed a standard mixed formulation, based on an independent interpolation for the membrane displacement w, the Airy stress function ϕ, and their Laplacians, $l^{[w]} = \nabla^2 w$ and $l^{[\phi]} = \nabla^2 \phi$, respectively: $w = \sum_j W_j\,\psi_j$, $\phi = \sum_j \Phi_j\,\psi_j$, $l^{[w]} = \sum_j L_j^{[w]}\,\psi_j$ and $l^{[\phi]} = \sum_j L_j^{[\phi]}\,\psi_j$. The second

derivatives of w and ϕ in the nonlinear terms in the weak form of equations (2.8) and (2.9) cannot be integrated by parts. We therefore evaluated them using smoothed versions of the gradients $g_i^{[\{w,\phi\}]} = \partial\{w,\phi\}/\partial x_i$, which we expanded as $g_i^{[\{w,\phi\}]} = \sum_j \{\mathtt{W}_{ij}, \mathtt{F}_{ij}\}\,\psi_j$, obtaining the coefficients $\mathtt{W}_{ij}$ and $\mathtt{F}_{ij}$ from the projection equations

$$r_{ij}^{[\{\mathtt{W},\mathtt{F}\}]} = \int_\Omega \left(\frac{\partial\{w,\phi\}}{\partial x_i} - g_i^{[\{w,\phi\}]} \right)\psi_j\,dx_1\,dx_2 = 0, \tag{3.5}$$

where $\Omega = \Omega_{\text{fluid}} \cup \Omega_{\text{air}}$. The weak form of (2.9) then yields the residuals

$$r_j^{[\phi]} = \int_\Omega \left(\frac{\partial l^{[\phi]}}{\partial x_k}\frac{\partial\psi_j}{\partial x_k} - \left[\frac{\partial g_1^{[w]}}{\partial x_1}\frac{\partial g_2^{[w]}}{\partial x_2} - \frac{1}{4}\left(\frac{\partial g_1^{[w]}}{\partial x_2} + \frac{\partial g_2^{[w]}}{\partial x_1} \right)^2 \right]\psi_j \right)dx_1\,dx_2 = 0, \tag{3.6}$$

which we treated as the equation for the unknown nodal values of the Airy stress function, Φ_j. Similarly, we used the residuals associated with the weak form of equation (2.8),

$$r_j^{[w]} = \int_\Omega \left(\eta\left[\frac{\partial g_2^{[\phi]}}{\partial x_2}\frac{\partial g_1^{[w]}}{\partial x_1} + \frac{\partial g_1^{[\phi]}}{\partial x_1}\frac{\partial g_2^{[w]}}{\partial x_2} - \frac{1}{2}\left(\frac{\partial g_1^{[w]}}{\partial x_2} + \frac{\partial g_2^{[w]}}{\partial x_1} \right)\left(\frac{\partial g_1^{[\phi]}}{\partial x_2} + \frac{\partial g_2^{[\phi]}}{\partial x_1} \right) \right]\psi_j + \right.$$

$$\left. + \frac{\partial l^{[w]}}{\partial x_k}\frac{\partial\psi_j}{\partial x_k} + P\,\psi_j \right)dx_1\,dx_2 = 0, \tag{3.7}$$

as the equation that determines the nodal values of the membrane displacements, W_j. Finally, the Laplacians of w and ϕ were determined from the integrated-by-parts projection equations

$$r_j^{[\{l^{[w]},\,l^{[\phi]}\}]} = \int_\Omega \left(\frac{\partial\{w,\phi\}}{\partial x_k}\frac{\partial\psi_j}{\partial x_k} + l^{[\{w,\phi\}]}\,\psi_j \right)dx_1\,dx_2 = 0. \tag{3.8}$$

The boundary terms that arise during the integration by parts in the derivation of equations (3.6)-(3.8) vanish because of the homogeneous boundary conditions (2.10).

We discretised the time-derivatives in the above equations using a second-order accurate, adaptive BDF scheme. The time step was adjusted based on the error estimate for the position of the air-liquid interface. The mesh velocity was taken into account when evaluating the (Eulerian) time derivative of b in (3.2). To avoid strong distortion of elements in the moving mesh, the mesh was re-generated every few timesteps. Spatial error estimates, obtained from Z2 flux recovery error estimator (Zienkiewicz & Zhu 1992), were used to refine/coarsen the mesh in regions of large/small pressure gradients. All fields were transferred between the meshes by projection.

The nonlinear algebraic equations listed above were solved "monolithically" by Newton's method. We used the sparse direct solver SuperLU (Demmel *et al.* 1999) to solve the large systems of linear algebraic equations for the Newton corrections. The number of discrete unknowns varied throughout the simulations, but reached up to 130,000.

Computations were performed in a two-stage procedure. To generate a well-defined geometric perturbation to the air-liquid interface we initially set $\mathcal{I} = 0$ to ensure that the membrane remained in its undeformed position. We then solved the steady equations, obtained by setting all time-derivatives to zero, while applying a pressure perturbation, $\varepsilon_P \cos(N\theta)$, to the bubble pressure in the dynamic boundary condition (2.6). The value of ε_P necessary to generate a geometric perturbation of the required amplitude was obtained from the linearised version of equation (2.6). The resulting steady solution was then used as the initial condition for the subsequent unsteady simulation during which we set $\varepsilon_P = 0$ and reset $\mathcal{I}$ to its desired value. We note that this procedure closely resembles the experimental protocol used by Pihler-Puzović *et al.* (2012).
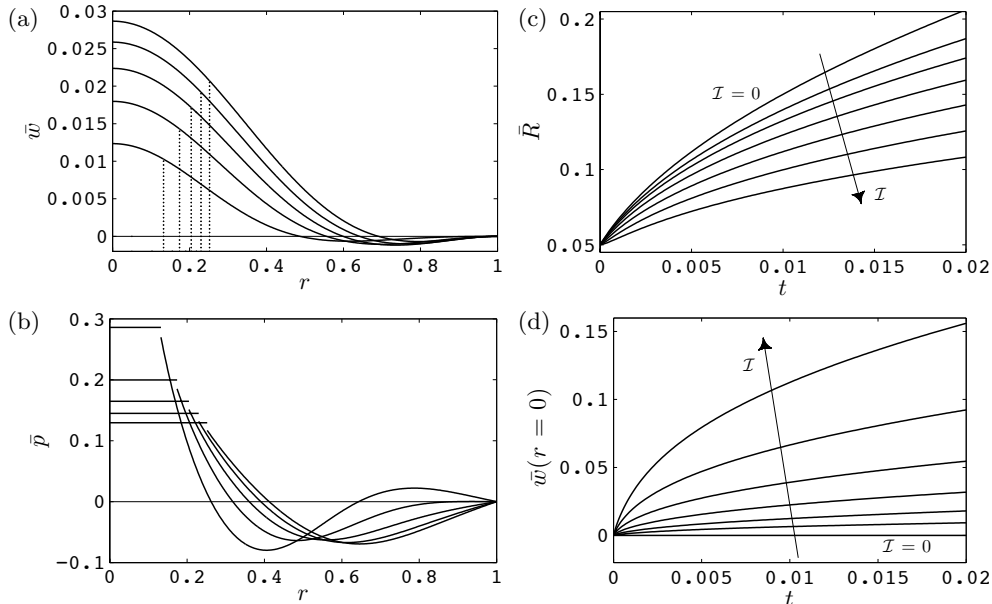
FIGURE 3. Instantaneous (a) membrane profiles and (b) pressures for $\mathcal{I} = 10^2$ at $t = 0.01$, 0.02, 0.03, 0.04 and 0.05. The dotted lines in (a) indicate the position of the air-liquid interface at the given times. Variation of (c) the position of the interface, $\bar{R}$, and (d) the deflection of the membrane at the centre of the cell, $\bar{w}(r = 0)$, with time, t, for $\mathcal{I} = 0$, 10, 10^2, 10^3, 10^4, 10^5 and 10^6. The direction of increasing $\mathcal{I}$ is indicated by the arrow.

4. Results

The problem is governed by four non-dimensional parameters: the aspect ratio $\mathcal{A}$, the capillary number Ca, the Föppl-von Kármán parameter η, and the FSI parameter $\mathcal{I}$. Since the main aim of our study is to explore the effect of wall elasticity on the viscous fingering instability we focus on variations in the FSI parameter $\mathcal{I}$, keeping all other parameters constant. This can be interpreted as a variation in the elastic modulus of the membrane with $\mathcal{I} = 0$ corresponding to a rigid-walled cell. Throughout this section we set the other parameters to $\mathcal{A} = 0.04$, $Ca^{-1} = 2.5685$ and $\eta = 10^2$. The choice of parameter values and the effect of their variation will be discussed in more detail in §6.

We ensured that the numerical results presented below are fully converged (in the sense that an increase in the spatial or temporal resolution gives graphically indistinguishable results) by repeating selected computations with smaller timesteps and element sizes; see Fig. 8 in Appendix A for a representative result.

4.1. *The axisymmetric solution*

The axisymmetric evolution of the system is illustrated in Fig. 3. The solid lines in Fig. 3 (a) show the shape of the elastic membrane at five equally-spaced instants, while the dotted vertical lines indicate the corresponding position of the air-liquid interface. The behaviour shown in this graph is fairly typical for all simulations performed in our study: the continuously increasing volume of the air bubble is accommodated by the increase in the bubble radius and the simultaneous inflation of the bounding membrane. Fig. 3 (b) shows the radial pressure distribution at the same instants as in Fig. 3 (a). The position of the air-liquid interface is clearly visible by the capillary pressure jump. The

bubble pressure decreases continuously as the bubble grows. The transverse deflection of the membrane ($\partial b/\partial t \neq 0$) has a noticeable effect on the velocity in the viscous fluid. In the rigid-walled case the injection of air creates a positive radial velocity (identifiable by $\partial p/\partial r < 0$; see (2.4)) throughout the Hele-Shaw cell. The plot of the pressure distribution in the elastic-walled Hele-Shaw cell in Fig. 3 (b) shows positive and negative radial velocities, indicating that the fluid required to occupy the expanding gap under the inflating membrane is partially recruited from the region ahead of the expanding bubble.

The evolution of the bubble radius, $\bar{R}(t)$, is shown in Fig. 3 (c) for different values of the FSI parameter $\mathcal{I}$. For $\mathcal{I} = 0$ (corresponding to a rigid-walled Hele-Shaw cell) the bubble radius follows directly from volume conservation and is given by $\bar{R}(t) = \sqrt{R_{\text{init}}^2 + 2t}$. An increase in $\mathcal{I}$ (while keeping all other parameters constant) can be interpreted as a reduction in the membrane's Young's modulus. This leads to a larger deflection of the membrane (see also the plot of the maximum deflection, $\bar{w}(r = 0, t)$, in Fig. 3 (d)) and thus reduces the growth rate of the bubble radius. The evolution of the bubble radius $\bar{R}(t)$ shown in Fig. 3 (c) is well described by a power law, $\bar{R} \sim t^\alpha$, where the exponent α decreases with an increase in $\mathcal{I}$. This is consistent with the findings of Pihler-Puzović *et al.* (2012) and Lister *et al.* (2013).

4.2. *Non-axisymmetric instabilities and fingering*

4.2.1. *Linear stability analysis*

Next we consider the stability of the evolving axisymmetric system to non-axisymmetric perturbations. Following Paterson (1981), we assess the stability of the axisymmetrically growing bubble by analysing the instantaneous growth rate of small-amplitude non-axisymmetric perturbations to the bubble radius. For a rigid-walled, finite-size cell the growth rate of perturbations with azimuthal wavenumber N is given by

$$\frac{1}{\hat{R}}\frac{\text{d}\hat{R}}{\text{dt}} = \frac{1}{\bar{R}^2}\left[\frac{N}{\bar{R}}\left(\frac{1}{12}Ca^{-1}\mathcal{A}^2(1 - N^2) + \bar{R}\right)\frac{1 + \bar{R}^{2N}}{1 - \bar{R}^{2N}} - 1\right]. \tag{4.1}$$

The growth rate depends not only on the wavenumber N but also on the instantaneous radius $\bar{R}(t)$ of the axisymmetric air-liquid interface, implying that the most unstable perturbation may change during the system's evolution.

We note that a decrease in Ca (which corresponds to an increase in the surface tension or a decrease in the injection flow rate) reduces $1/\hat{R}\,\text{d}\hat{R}/\text{dt}$, and is therefore stabilising. However, as in the case of an infinitely large Hele Shaw cell considered by Paterson (1981), the axisymmetrically evolving system always becomes unstable to non-axisymmetric perturbations at some point in its evolution – there is no "critical flow rate" (or capillary number) below which the non-axisymmetric instabilities are suppressed.

For the parameter values chosen in the simulations in Fig. 4 (a), the axisymmetric initial configuration is immediately unstable to non-axisymmetric perturbations with a range of wavenumbers. When $\bar{R} = \bar{R}(t = 0) = \bar{R}_{\text{init}} = 0.05$, the most rapidly growing mode in a rigid-walled cell ($\mathcal{I} = 0$) has wavenumber $N = 7$. The topmost line in Fig. 4 (a) shows the evolution of this mode's growth rate as a function of the radius of the axisymmetric bubble, $\bar{R}(t)$. The growth rate decreases continuously but always remains positive. The other lines in this figure show corresponding results (for the same wavenumber) for the elastic-walled case. An increase in $\mathcal{I}$ decreases the growth rate of the non-axisymmetric perturbations. For $\mathcal{I} = 10^4$ the axisymmetric state is stable initially, becomes unstable between $\bar{R} = 0.052$ and $\bar{R} = 0.084$ but then restabilises, illustrating that the instabilities in the elastic-walled cell are in general transient. Finally, for $\mathcal{I} = 10^5$, the axisymmetric state remains stable to non-axisymmetric perturbations of the given wavenumber over the whole range of radii shown.
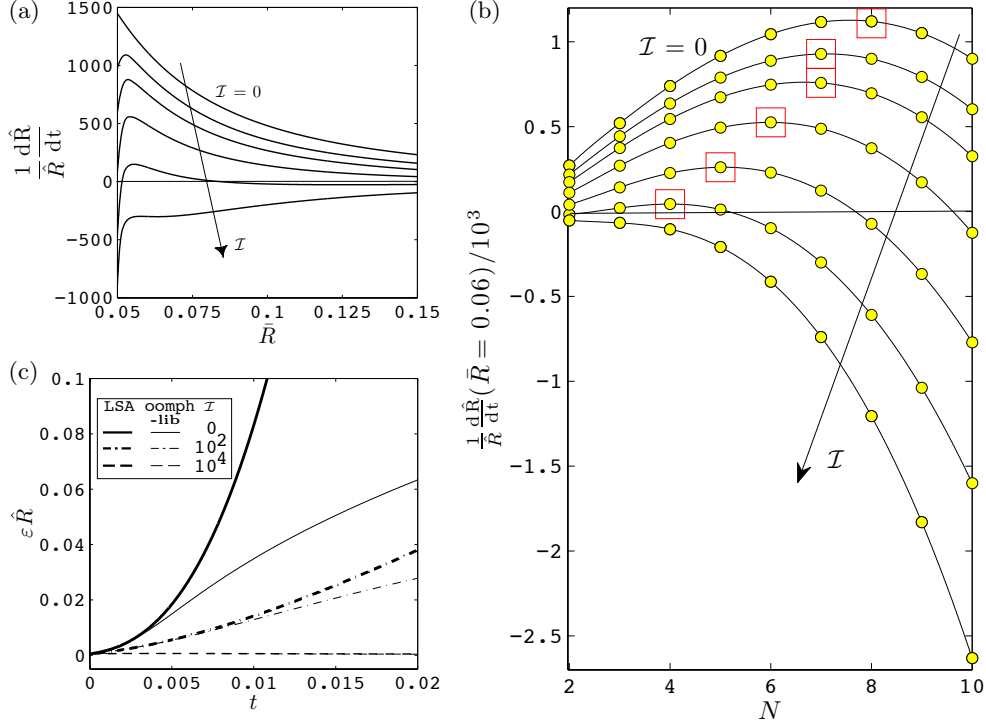
FIGURE 4. (a) Evolution of the growth rates of the non-axisymmetric instability as a function of the radius $\bar{R}$ for $N = 7$ and $\mathcal{I} = 0$, 10, 10^2, 10^3, 10^4 and 10^5. (b) The growth rates at a fixed radius $\bar{R} = 0.06$ as a function of the wavenumber N for $\mathcal{I} = 0, 10, 10^2, 10^3, 10^4, 10^5$ and 10^6, indicated by small yellow circles, connected by a spline for easier visualisation. The most unstable mode for a given $\mathcal{I}$ is highlighted by the square symbol, except for $\mathcal{I} = 10^6$, for which all growth rates are negative. (c) Comparison of the linear stability analysis (LSA) and the nonlinear simulations (`oomph-lib`) by plotting the time-evolution of $\varepsilon\hat{R}$ for $N = 7$. The direction of increasing $\mathcal{I}$ is indicated by the arrow.

(a) Dendritic fingers: (b) Stubby fingers: (c) Suppressed fingers: (d) Sheet displacement:
$\mathcal{I} = 0$ $\mathcal{I} = 10^2$ $\mathcal{I} = 10^4$ $\mathcal{I} = 10^2$
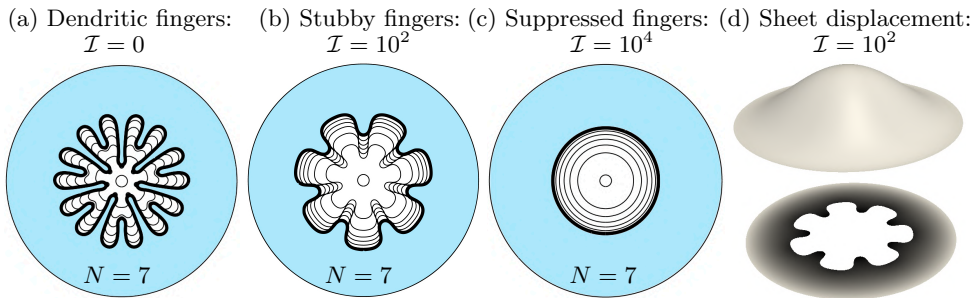
FIGURE 5. (a)-(c) Top view of seven successive positions of the air-liquid interface, with the smallest shown at $t = 0$, the last one highlighted with the bold line and increments of (a) $\Delta t = 0.017$; (b) $\Delta t = 0.063$; (c) $\Delta t = 0.083$. (d) The shape of the membrane (transverse displacement increased by a factor of 5) and the pressure field in the fluid (darker regions correspond to larger pressures in the range $[0, 0.068]$) at $t = 0.38$ for $\mathcal{I} = 10^2$.
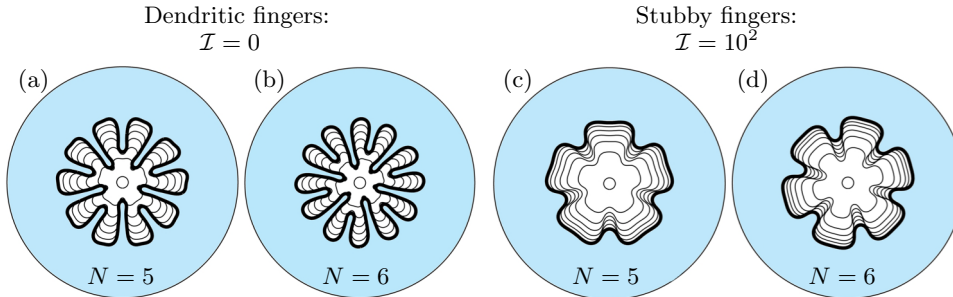
FIGURE 6. Top view of seven successive positions of the air-liquid interface, with the smallest shown at $t = 0$, the last one highlighted with the bold line and (a) $\Delta t = 0.017$, (b) $\Delta t = 0.016$, (c) $\Delta t = 0.048$ and (d) $\Delta t = 0.058$.

So far we have only considered the effect of variations in $\mathcal{I}$ on the growth rate of perturbation with the fixed wavenumber, $N = 7$, that results in the most rapid initial growth in the rigid-walled cell. To assess the effect of wall elasticity on the growth rates of other modes, in Fig. 4 (b) we plot the growth rate of perturbations with different wavenumbers at a fixed radius, $\bar{R} = 0.06$ (close to the radius at which the growth rate of the instabilities tends to be largest; see Fig. 4 (a)), for different values of $\mathcal{I}$. The red squares identify the maximum growth rate for each $\mathcal{I}$ and show that an increase in $\mathcal{I}$ decreases the most unstable wavenumber. For sufficiently large values of $\mathcal{I}$ the growth rates of all perturbations become negative, implying complete suppression of the fingering instability.

We note that the maxima in the growth rate curves for fixed $\mathcal{I}$ are fairly shallow. This implies that a large number of linearly unstable modes have comparable growth rates, suggesting that the number of large-amplitude fingers that will ultimately emanate from the linear instability will depend sensitively on the wavenumber(s) of the initial perturbation.

4.2.2. Large-amplitude fingering

The dependence of the growth rate on both time (via $\bar{R}(t)$) and the wavenumber N, makes it difficult to assess which of the (typically many) linearly unstable modes are likely to evolve into the finite-amplitude fingers observed in the experiments. Furthermore, the competition and interaction between different modes is impossible to explore using a linearised (small-amplitude) analysis. To assess the range of validity of the linearised analysis, Fig. 4 (c) shows the amplitude of the perturbation to the axisymmetric interface, $\varepsilon\hat{R}(t)$, predicted by the linear stability analysis (thick lines) and the direct numerical simulation of the full, nonlinear equations with `oomph-lib` (thin lines), for a rigid-walled and two elastic-walled cells. The three simulations were started from the same initial radius and used the same small-amplitude perturbation $\varepsilon\hat{R}(t = 0)/R_{\text{init}} = 0.01$ with wavenumber $N = 7$. For $\mathcal{I} = 0$ and $\mathcal{I} = 10^2$ the system initially exhibits approximately exponential growth, but nonlinear effects lead to a rapid saturation when $\varepsilon\hat{R}(t) \gtrsim 0.006$. For $\mathcal{I} = 10^4$ the linear stability analysis predicted a short transient period of growth (while $0.052 < \bar{R}(t) < 0.084$; see Fig. 4 (a)). Fig. 4 (c) shows that this transient instability produces only very small perturbations to the axisymmetric state so that $\varepsilon\hat{R}(t)$ remains close to zero throughout the system's evolution.

The nonlinear evolution of the air-liquid interface for the three values of $\mathcal{I}$ is illustrated in more detail in Fig. 5 (a-c). In each sub-figure, the various lines show the position of

the air-liquid interface at fixed time-intervals (specified by the value of Δt). In all cases we applied an initial perturbation with wavenumber $N = 7$ and amplitude $\varepsilon \hat{R}(t = 0)/R_{\text{init}} = 0.01$ to the air-liquid interface. This initial perturbation develops rapidly into large-amplitude fingers, whose shape depends on the value of $\mathcal{I}$. For the rigid-walled case we obtain the characteristic dendritic fingering pattern in which the bases of the fingers only move very slowly while the finger tips continue to grow outwards and split when they have become sufficiently wide. In the elastic-walled case with $\mathcal{I} = 10^2$ (Fig. 5 (b)) the large-amplitude fingers look fundamentally different and adopt the "short stubby" shape observed in the experiments because their bases continue to propagate outwards. Finally, for sufficiently large values of $\mathcal{I}$ fingering is either completely suppressed or the short transient growth of non-axisymmetric instabilities is so weak that viscous fingering is effectively suppressed, as in Fig. 5 (c) for $\mathcal{I} = 10^4$. The initial perturbation ultimately decays and the interface returns to a slowly expanding axisymmetric shape.

In Fig. 5 (d) we show the shape of the membrane (with the transverse displacement increased by a factor of 5) at $t = 0.38$ for the case $\mathcal{I} = 10^2$. Note that although the air-liquid interface has already developed large-amplitude fingers and the pressure in the viscous fluid is highly non-uniform, the deformation of the membrane remains very close to axisymmetric.

The dependence of the large-amplitude fingers on the wavenumber of the initial perturbation is explored in Fig. 6, which shows the nonlinear evolution of the air-liquid interface for the same parameter values as in Figs. 5 (a,b) (for $\mathcal{I} = 0$ and $\mathcal{I} = 10^2$, respectively). In the linear stability analysis the $N = 7$ mode was found to have the largest initial growth rate for both of these cases and was therefore used as the wavenumber of the initial perturbation for the simulations in Fig. 5. In Fig. 6 we show the system's evolution if the wavenumber of the initial perturbation is changed to $N = 5$ and $N = 6$, using the same amplitude (1% of the initial radius) as in Fig. 5. The results show that even such small perturbations suffice to generate large-amplitude fingers with a wavenumber that differs from the most unstable wavenumber of the intial configuration, despite the fact that imperfections in the unstructured computational mesh excite a large spectrum of modes. This is consistent with the relatively flat maximum of the growth rate vs wavenumber curves in Fig. 4 (b) that we already alluded to in §4.2.1.

5. The mechanism for suppression of fingering

The results presented in the last section indicate that the viscous potential flow model developed in §2 is capable of predicting the experimentally observed behaviour. Its relative simplicity makes it possible to gain insight into the mechanism by which the presence of wall elasticity suppresses the viscous fingering.

First we recall the physical mechanism responsible for fingering in the rigid parallel-walled Hele-Shaw cell. For convenience we will present the argument for the case of a planar cell in which air (at a spatially constant pressure p_B) displaces a thin layer of viscous fluid in an infinitely wide channel – the setup originally studied by Saffman & Taylor (1958) (Fig. 7 (a, b)). Assuming that the viscous fluid leaves the channel far ahead of the air-liquid interface at a constant pressure, p_∞, the flow of the viscous fluid is driven by the instantaneous pressure gradient $\nabla p = (p_\infty - p_B)/\bar{L} \; \mathbf{e}_x$. If the position of the air-liquid interface is disturbed slightly, so that $L = \bar{L} + \varepsilon \cos(Ny)$ (as shown in Fig. 7 (b)), the pressure gradient – and via (2.3) the velocity of the interface – is increased [decreased] in regions where the interface protrudes from [lags behind] its average position $\bar{L}$. The resulting instability is counteracted by capillary effects: the pressure gradient induced by the in-plane curvature $\kappa_\parallel$ in (2.6) aims to straighten the interface. In the rigid-walled

Parallel-sided channel

(a)

$b = const$

p_B

$\bar{\kappa}_\parallel \equiv 0$
$\bar{\kappa}_\perp \equiv \frac{2}{b}$

$\bar{L}$

p_∞

(b)

$\bar{L} + \varepsilon$

$\bar{L} - \varepsilon$

p_B

$\kappa_\parallel < \bar{\kappa}_\parallel$
$\kappa_\perp \equiv \bar{\kappa}_\perp$

$\kappa_\parallel > \bar{\kappa}_\parallel$
$\kappa_\perp \equiv \bar{\kappa}_\perp$

p_∞

Tapered channel

(c)

$\frac{\partial b}{\partial x} \neq 0$

p_B

$\bar{\kappa}_\parallel \equiv 0$
$\bar{\kappa}_\perp \equiv \frac{2}{b}$

p_∞

(d)

p_B

$\kappa_\parallel < \bar{\kappa}_\parallel$
$\kappa_\perp < \bar{\kappa}_\perp$

$\kappa_\parallel > \bar{\kappa}_\parallel$
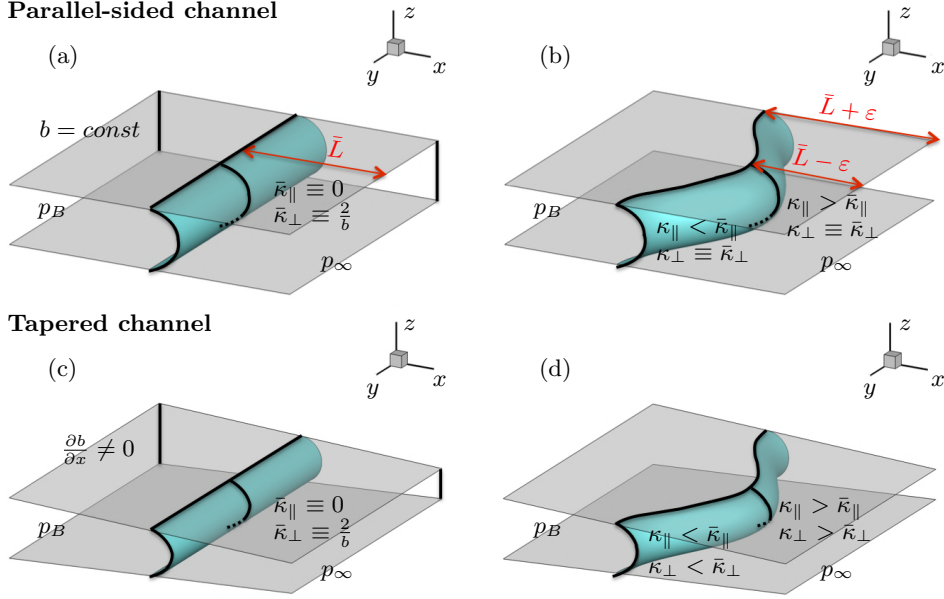$\kappa_\perp > \bar{\kappa}_\perp$

p_∞

FIGURE 7. Diagram showing (a, c) the unperturbed and (b, d) perturbed air-liquid interface in (a, b) a parallel-sided and (c, d) tapered rectangular channel. Note how the taper increases [decreases] the transverse curvature of the air-liquid interface and the viscous resistance in regions where it protrudes [lags behind] its mean position.

cell, fingering is therefore controlled by the relative importance of (destabilising) viscous and (stabilising) capillary effects. Note that in the simple approximation (2.7) for the mean curvature, the (larger) transverse curvature, $\kappa_\perp = 2/b \gg \kappa_\parallel$ does not contribute to the dynamics of the interface because $b = const$.

The introduction of wall elasticity alters the two-phase flow in the Hele-Shaw cell in two significant ways: (a) the velocity of the air-liquid interface is reduced because a fraction of the injected volume of air is accomodated by the deflection of the elastic upper boundary (see Fig. 3); (b) the inflation of the Hele-Shaw cell (which is largest at the centre; see Fig. 3) implies that the air-liquid interface generally propagates into a converging fluid-filled gap (as in the case considered by Reinelt (1995)), i.e. b decreases in the direction of the flow as shown in Fig. 7 (c, d) (again for the planar case). These observations suggest at least three mechanisms by which the presence of the elastic membrane weakens the viscous fingering instability: (i) the increase [decrease] in the transverse component of the interface curvature ($\kappa_\perp = 2/b$) in regions of the air-liquid interface that protrude from [lag behind] its mean position leads to an increase in the restoring capillary forces; (ii) the reduction in the interface speed reduces the destabilising viscous effects; (iii) the destabilising effect of an increase [decrease] in the driving pressure gradient is counteracted by the decrease [increase] in b since the normal velocity of the interface is proportional to $|b^2 \nabla p|$ (see equation (2.4)).

In order to assess the relative importance of viscous [(ii), (iii)] and capillary [(i)] stabilising effects, we neglected the transverse curvature term ($\kappa_\perp = 2/b$) in the dynamic boundary condition (2.6) and repeated the entire linear stability analysis (comprising the computation of the axisymmetric base flow and the growth rate of small-amplitude non-axisymmetric perturbations). The resulting predictions for the growth rate $1/\hat{R} \, d\hat{R}/dt$, shown with big gray circles in Fig. 8 (a), agree extremely well with the predictions from
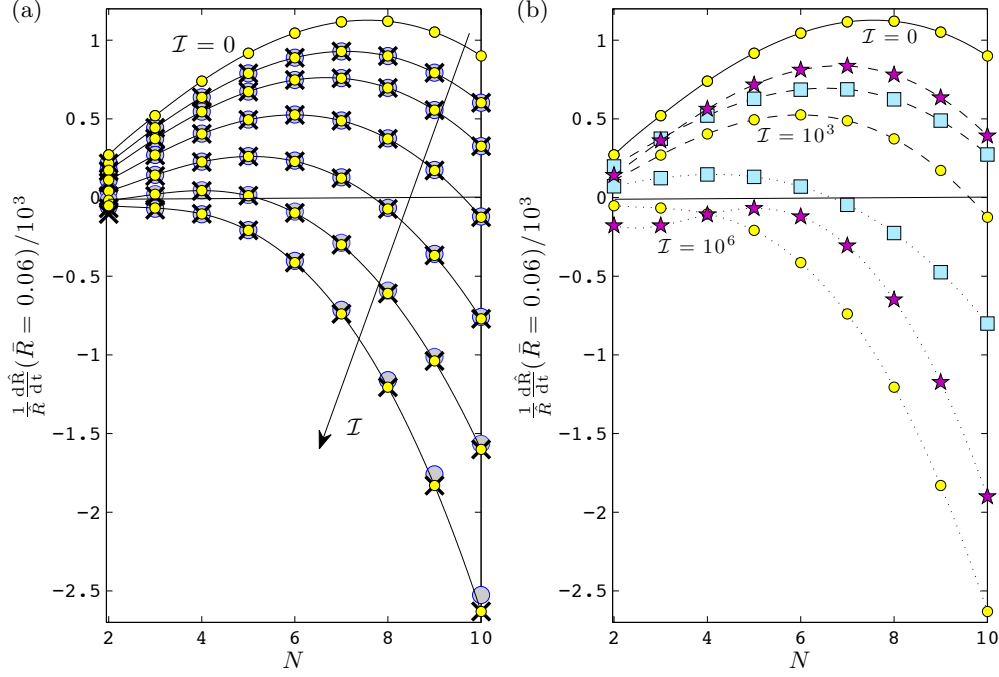
FIGURE 8. (a) Growth rates at a fixed radius $\bar{R} = 0.06$ as a function of the wavenumber N. The direction of increasing $\mathcal{I}$ is indicated by the arrow. Small yellow circles correspond to the results from the full analysis (repeated from Fig. 4 (b)). Big gray circles and crosses show results obtained when neglected the effect of the transverse interface curvature (by setting $\kappa_\perp = 0$), and by ignoring non-axisymmetric perturbations to the wall shape (by setting $\hat{w} = \hat{\phi} = 0$), respectively. (b) Purple stars show the growth rates in a rigid cell, in which the interface propagates at the same velocity as the interface in the corresponding elastic cell; blue squares show the growth rates in an elastic cell, in which the interface propagates at the same velocity as the interface in the rigid cell.

the full model (small yellow circle), indicating that the capillary effects play only a very minor role in the suppression of viscous fingering – at least for the parameter values considered here.

The analysis presented so far has neglected the fact that the onset of instabilities deforms both the air-liquid interface and the elastic membrane. It is difficult to assess *a priori* if perturbations to the shape of the membrane have a stabilising or destabilising effect on the fingering instability. We therefore performed the stability analysis for a third time, this time using the full equations (which include the transverse interface curvature) for the computation of the axisymmetric base state, but neglecting the perturbation to the membrane shape (by setting $\hat{w} = \hat{\phi} = 0$) when computing the growth rate of the non-axisymmetric perturbations. The resulting predictions for the growth rate $1/\hat{R} \, d\hat{R}/dt$ are indicated by crosses in Fig. 8 (a). Again they agree extremely well with the predictions from the full model. This is consistent with our observation that the non-axisymmetric perturbations to the membrane shape tend to be relatively small, even in cases when the viscous fingers have grown to a large amplitude (see, e.g., Fig. 5 (d)). Therefore, we conclude that the suppression of viscous fingering by fluid-structure interaction arises predominantly through the two viscous effects: (i) the inflation of the bounding membrane

reduces the speed at which the axisymmetric air bubble expands and therefore reduces the destabilising viscous forces and/or (ii) the inflation of the membrane increases the viscous resistance to fingers that protrude further into the converging gap between the upper and lower boundaries of the Hele-Shaw cell. For sufficiently elastic membranes the combination of the two effects is strong enough to suppress viscous fingering altogether.

In an attempt to assess the relative importance of the two viscous effects, we show in Fig. 8 (b) the variation of the growth rate with the wavenumber for three values of the FSI parameter $\mathcal{I}$. The figure contrasts the predictions from the full model (identified by the circular markers) with the growth rates obtained from two alternative models, each designed to remove (approximately) one of the two stabilising viscous effects. Firstly, to suppress the deceleration of the air-liquid interface caused by the inflation of the elastic membrane (which is responsible for the stabilisation via mechanism (i)) we replace the volume constraint (2.2) by the condition that the velocity of the axisymmetric air-liquid interface matches that of the axisymmetrically expanding air bubble in the corresponding rigid-walled cell, or, in other words, is equal to $1/\sqrt{R_{\mathrm{init}}^2 + 2t}$. The growth rates obtained from the linear stability analysis of that problem are indicated by the star-shaped markers in Fig. 8 (b). Secondly, to suppress the variation in the gap width (which is responsible for the stabilisation by mechanism (ii)), we performed the linear stability analysis for a rigid-walled cell but imposed the velocity of the axisymmetric air-liquid interface to match that in the corresponding elastic-walled system. The growth rates for that problem are indicated by the square markers in Fig. 8 (b).

The comparison of the growth rates from the three models shows that both viscous effects are capable of significantly reducing the growth rates of non-axisymmetric perturbations. However, at least for the parameter values considered here, neither effect appears to act in isolation and it would be difficult to claim that one is uniformly more important than the other.

Finally, we assessed the relative importance of the bending and stretching terms in the Föppl-von Kármán equations by repeating the stability analysis for a final time for $\eta = 0$, thus ignoring the self-induced membrane tension represented by the nonlinear terms in equations (2.8)-(2.9). The growth rates $1/\hat{R} \, \mathrm{d}\hat{R}/\mathrm{d}t$ were found to agree extremely well with the corresponding predictions for the default value of $\eta = 10^2$ used in all other computations, with a maximum difference of less than 1% in the growth rates for the cases shown in Fig. 8. This indicates that, for the parameter values considered here, the bending terms in (2.8)-(2.9) are dominant and the self-induced tension can be neglected. Additional computations showed that the self-induced membrane tension becomes significant for $\eta \geqslant 10^4$.

6. Summary and Discussion

We have developed a theoretical model for flows in elastic-walled Hele-Shaw cells by coupling the classical viscous potential flow model of Saffman & Taylor (1958) to the Föppl-von Kármán equations which describe the deformation of the elastic wall. Our model not only captures qualitatively all the features observed in the experiments by Pihler-Puzović *et al.* (2012), but also allows us to explain how the presence of wall elasticity alters (or even suppresses) the viscous fingering instability that arises in rigid-walled cells. The key feature is that in an elastic-walled cell, the axisymmetric inflation of the membrane prior to the onset of the instability reduces the growth rate of the expanding air bubble (because the axisymmetrically expending air-liquid interface slows down compared to the interface in a rigid cell) and the air-liquid interface propagates into the narrowing fluid-filled gap. Both effects reduce the strength of the (viscous)

destabilising mechanism that is the primary driver for the fingering instability. Capillary effects and non-axisymmetric wall deformations only play a minor role in the onset of the instability. The stabilising mechanism identified here is therefore fundamentally different from the capillary mechanism responsible for the suppression of viscous fingering in tapered rigid-walled cells analysed by Al Housseiny *et al.* (2012).

While the "short and stubby" fingers that develop in our nonlinear simulations resemble those observed in the experiments, we have not yet performed any quantitative comparisons between our computational simulations and the experiments reported in Pihler-Puzović *et al.* (2012). This is partly because the main aim of the present paper was to identify the mechanism by which fluid-structure interaction, characterised by the FSI parameter $\mathcal{I}$, stabilises the fingering instability. In dimensional terms, variations in $\mathcal{I}$ (for constant Ca, η and $\mathcal{A}$) correspond to variations in the Young's modulus of the bounding membrane while keeping all other physical parameters, such as the injection flow rate $\dot{V}$, constant. This parameter variation differs from that employed in the experimental study of Pihler-Puzović *et al.* (2012), which focused on the determination of the growth rate of the fingering instability as a function of the injection flow rate $\dot{V}$, keeping all other physical parameters, such as Young's modulus, constant. The simulation/analysis of such experiments is feasible with our model but would require simultaneous variations in Ca and $\mathcal{I}$ since both parameters depend linearly on $\dot{V}$. Another difference between the computations presented here and the experiments reported by Pihler-Puzović *et al.* (2012) is that the instabilities observed under experimental conditions resulted in a relatively large numbers of fingers whose nonlinear growth would have been very costly to simulate. We therefore used the results of our linear stability analysis to adjust some of the parameters to reduce the most unstable wavenumbers for the computations presented in this paper. Compared to the range of parameters used in the experiments ($\mathcal{A} = 0.002 - 0.006$, $Ca^{-1} = 0.4 - 25$, $\eta = 2.5 \times 10^5 - 2.5 \times 10^6$ and $\mathcal{I} = 5 \times 10^4 - 6.5 \times 10^8$), we decreased the number of fingers by increasing the aspect ratio $\mathcal{A}$. This required a reduction of the Föppl-von Kármán parameter η to avoid the occurrence of wrinkling in the membrane ahead of the air-liquid interface. We note that such wrinkling is not a numerical artefact but has, in fact, been observed in more recent experiments with thinner sheets. The interaction between membrane wrinkling and viscous fingering is the subject of ongoing work and will be reported elsewhere.

Appendix A. Convergence tests

In Fig. 9 we present the results of a representative mesh convergence test. Fig. 9(a) shows the position of the air-liquid interface at an instant when the fingers have grown to large amplitude. Fig. 9(b) shows the time-evolution of the bubble pressure $p_\mathrm{B}(t)$ and the mean radius

$$R_\mathrm{mean}(t) = \frac{1}{\ell(t)} \int_0^{\ell(t)} \mathbf{R}(S,t) \cdot \mathbf{e}_r \, dS, \qquad (A\,1)$$

where $\ell(t)$ is the total arclength of the air-liquid interface. Solid lines represent results obtained with our standard spatial resolution; the dashed lines were obtained from a computation in which the number of elements was increased approximately five-fold. The results are graphically indistinguishable.
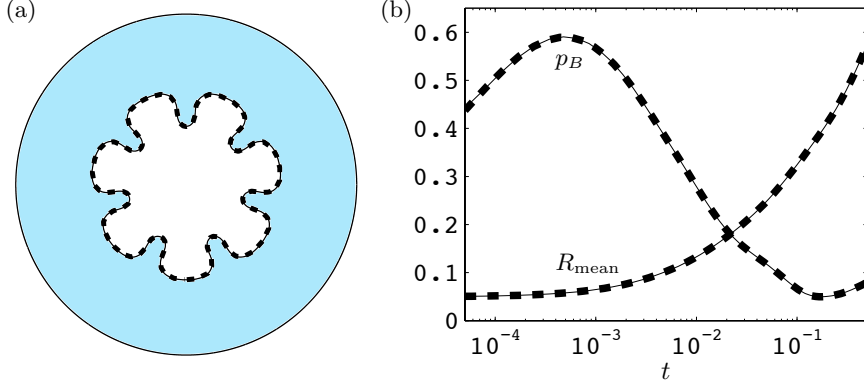
FIGURE 9. (a) Plot of the interface position at $t = 0.38$, and (b) time evolution of the mean interface radius, $R_{\mathrm{mean}}(t)$, and pressure in the air bubble, $p_B(t)$, obtained with the standard spatial resolution (solid lines) and with an approximately five-fold increase in the number of elements (dashed lines). $\mathcal{I} = 10^2$.

Appendix B. Equations used in the linear stability analysis

B.1. *The axisymmetric base state*

The nonlinear system of PDEs for the evolving axisymmetric base state $[\bar{p}(r,t),\ \bar{w}(r,t),\ \bar{\phi}(r,t),\ \bar{R}(t),\ p_B(t)]$ is

$$\left(1 + \frac{\bar{w}}{\mathcal{A}}\right)^3 \left(\frac{\partial^2 \bar{p}}{\partial r^2} + \frac{1}{r}\frac{\partial \bar{p}}{\partial r}\right) + 3\left(1 + \frac{\bar{w}}{\mathcal{A}}\right)^2 \frac{1}{\mathcal{A}}\frac{\partial \bar{w}}{\partial r}\frac{\partial \bar{p}}{\partial r} = \frac{1}{\mathcal{A}}\frac{\partial \bar{w}}{\partial t} \quad \text{for} \quad r \in [\bar{R}(t), 1], \quad (\mathrm{B}\,1)$$

$$\left[\frac{\partial^4 \bar{w}}{\partial r^4} + \frac{2}{r}\frac{\partial^3 \bar{w}}{\partial r^3} - \frac{1}{r^2}\frac{\partial^2 \bar{w}}{\partial r^2} + \frac{1}{r^3}\frac{\partial \bar{w}}{\partial r}\right] - \frac{\eta}{r}\left(\frac{\partial^2 \bar{w}}{\partial r^2}\frac{\partial \bar{\phi}}{\partial r} + \frac{\partial^2 \bar{\phi}}{\partial r^2}\frac{\partial \bar{w}}{\partial r}\right)$$
$$= \begin{cases} \mathcal{I} p_B(t) & \text{for } r \in [0, \bar{R}(t)), \\ \mathcal{I} \bar{p}(r,t) & \text{for } r \in [\bar{R}(t), 1], \end{cases} \quad (\mathrm{B}\,2)$$

$$\left[\frac{\partial^4 \bar{\phi}}{\partial r^4} + \frac{2}{r}\frac{\partial^3 \bar{\phi}}{\partial r^3} - \frac{1}{r^2}\frac{\partial^2 \bar{\phi}}{\partial r^2} + \frac{1}{r^3}\frac{\partial \bar{\phi}}{\partial r}\right] + \frac{1}{r}\frac{\partial^2 \bar{w}}{\partial r^2}\frac{\partial \bar{w}}{\partial r} = 0. \quad (\mathrm{B}\,3)$$

These equations are subject to the boundary conditions

$$\bar{p}(\bar{R},t) = p_B(t) - \frac{1}{12}Ca^{-1}\mathcal{A}\left(\frac{\mathcal{A}}{\bar{R}} + \frac{2}{1 + \bar{w}(\bar{R},t)/\mathcal{A}}\right), \quad (\mathrm{B}\,4)$$

$$\bar{p}(1,t) = 0, \quad (\mathrm{B}\,5)$$

$$\frac{\mathrm{d}\bar{R}}{\mathrm{d}t} = -\left(1 + \frac{\bar{w}(\bar{R},t)}{\mathcal{A}}\right)^2 \frac{\partial \bar{p}}{\partial r}(\bar{R},t), \quad (\mathrm{B}\,6)$$

$$\frac{\partial \bar{w}}{\partial r}(0,t) = 0, \quad \frac{\partial^3 \bar{w}}{\partial r^3}(0,t) = 0, \quad \bar{w}(1,t) = 0, \quad \frac{\partial \bar{w}}{\partial r}(1,t) = 0, \quad (\mathrm{B}\,7)$$

$$\frac{\partial \bar{\phi}}{\partial r}(0,t) = 0, \quad \frac{\partial^3 \bar{\phi}}{\partial r^3}(0,t) = 0, \quad \bar{\phi}(1,t) = 0, \quad \frac{\partial \bar{\phi}}{\partial r}(1,t) = 0, \quad (\mathrm{B}\,8)$$

the volume constraint

$$\int_0^{\bar{R}(t)} \left(1 + \frac{\bar{w}(r,t)}{\mathcal{A}}\right) r\,dr = R_{\mathrm{init}}^2/2 + t, \quad (\mathrm{B}\,9)$$

and the initial conditions

$$\bar{R}(t=0) = R_{\text{init}}, \quad \text{and} \quad \bar{w}(t=0) = 0. \tag{B 10}$$

B.2. *The small-amplitude non-axisymmetric perturbations*

The amplitudes of the perturbation, $[\hat{p}(r,t), \hat{w}(r,t), \hat{\phi}(r,t), \hat{R}(t)]$ with azimuthal wavenumber N satisfy the system of linear PDEs

$$\frac{1}{\mathcal{A}} \frac{\partial \hat{w}}{\partial t} = \frac{3}{\mathcal{A}} \left(1 + \frac{\bar{w}}{\mathcal{A}}\right)^2 \left[\frac{\partial \bar{w}}{\partial r} \frac{\partial \hat{p}}{\partial r} + \frac{\partial \bar{p}}{\partial r} \frac{\partial \hat{w}}{\partial r} + \hat{w} \left(\frac{\partial^2 \bar{p}}{\partial r^2} + \frac{1}{r} \frac{\partial \bar{p}}{\partial r} \right) \right]$$

$$+ \left(1 + \frac{\bar{w}}{\mathcal{A}}\right)^3 \left[\frac{\partial^2 \hat{p}}{\partial r^2} - \frac{N^2}{r^2} \hat{p} + \frac{1}{r} \frac{\partial \hat{p}}{\partial r} \right] + \left(1 + \frac{\bar{w}}{\mathcal{A}}\right) \frac{6}{\mathcal{A}} \frac{\partial \bar{w}}{\partial r} \frac{\partial \bar{p}}{\partial r} \hat{w} \quad \text{for} \quad r \in [\bar{R}(t), 1], \tag{B 11}$$

$$\left[\frac{\partial^4 \hat{w}}{\partial r^4} + \frac{2}{r} \frac{\partial^3 \hat{w}}{\partial r^3} - \frac{1}{r^2} (1 + 2N^2) \frac{\partial^2 \hat{w}}{\partial r^2} + \frac{1}{r^3} (1 + 2N^2) \frac{\partial \hat{w}}{\partial r} + \frac{N^2}{r^4} (N^2 - 4) \hat{w} \right]$$

$$- \frac{\eta}{r} \left[\frac{\partial^2 \bar{\phi}}{\partial r^2} \frac{\partial \hat{w}}{\partial r} + \frac{\partial^2 \hat{\phi}}{\partial r^2} \frac{\partial \bar{w}}{\partial r} + \frac{\partial^2 \bar{w}}{\partial r^2} \frac{\partial \hat{\phi}}{\partial r} + \frac{\partial^2 \hat{w}}{\partial r^2} \frac{\partial \bar{\phi}}{\partial r} - \frac{N^2}{r} \left(\frac{\partial^2 \bar{w}}{\partial r^2} \hat{\phi} + \frac{\partial^2 \bar{\phi}}{\partial r^2} \hat{w} \right) \right]$$

$$= \begin{cases} 0 & \text{for } r \in [0, \bar{R}(t)), \\ \mathcal{I}\hat{p} & \text{for } r \in [\bar{R}(t), 1], \end{cases} \tag{B 12}$$

$$\left[\frac{\partial^4 \hat{\phi}}{\partial r^4} + \frac{2}{r} \frac{\partial^3 \hat{\phi}}{\partial r^3} - \frac{1}{r^2} (1 + 2N^2) \frac{\partial^2 \hat{\phi}}{\partial r^2} + \frac{1}{r^3} (1 + 2N^2) \frac{\partial \hat{\phi}}{\partial r} + \frac{N^2}{r^4} (N^2 - 4) \hat{\phi} \right]$$

$$+ \frac{1}{r} \left[\frac{\partial^2 \bar{w}}{\partial r^2} \frac{\partial \hat{w}}{\partial r} + \frac{\partial^2 \hat{w}}{\partial r^2} \frac{\partial \bar{w}}{\partial r} - \frac{N^2}{r} \frac{\partial^2 \bar{w}}{\partial r^2} \hat{w} \right] = 0. \tag{B 13}$$

They are subject to the boundary conditions

$$\frac{1}{12} Ca^{-1} \mathcal{A} \left(\mathcal{A} \frac{\hat{R}}{\bar{R}^2} (1 - N^2) + \frac{2}{\mathcal{A}} \frac{1}{\left(1 + \bar{w}(\bar{R}, t)/\mathcal{A}\right)^2} \left(\hat{w} + \hat{R} \frac{\partial \bar{w}}{\partial r} (\bar{R}, t) \right) \right)$$

$$- \hat{R} \frac{\partial \bar{p}}{\partial r} (\bar{R}, t) = \hat{p}(\bar{R}, t), \tag{B 14}$$

$$\hat{p}(1, t) = 0, \tag{B 15}$$

$$\frac{\mathrm{d}\hat{R}}{\mathrm{d}t} = - \left(1 + \frac{\bar{w}(\bar{R}, t)}{\mathcal{A}}\right)^2 \left[\hat{R} \frac{\partial^2 \bar{p}}{\partial r^2} (\bar{R}, t) + \frac{\partial \hat{p}}{\partial r} (\bar{R}, t) \right]$$

$$- \frac{2}{\mathcal{A}} \left(1 + \frac{\bar{w}(\bar{R}, t)}{\mathcal{A}}\right) \frac{\partial \bar{p}}{\partial r} (\bar{R}, t) \left[\hat{R} \frac{\partial \bar{w}}{\partial r} (\bar{R}, t) + \hat{w}(\bar{R}, t) \right], \tag{B 16}$$

$$\frac{\partial \hat{w}}{\partial r}(0, t) = 0, \quad \frac{\partial^3 \hat{w}}{\partial r^3}(0, t) = 0, \quad \hat{w}(1, t) = 0, \quad \frac{\partial \hat{w}}{\partial r}(1, t) = 0, \tag{B 17}$$

$$\frac{\partial \hat{\phi}}{\partial r}(0, t) = 0, \quad \frac{\partial^3 \hat{\phi}}{\partial r^3}(0, t) = 0, \quad \hat{\phi}(1, t) = 0, \quad \frac{\partial \hat{\phi}}{\partial r}(1, t) = 0, \tag{B 18}$$

and the initial conditions

$$\hat{R}(t=0) = 1, \quad \text{and} \quad \hat{w}(t=0) = 0. \tag{B 19}$$

REFERENCES

BEN JACOB, E., SCHMUELI, H., SHOCHET, O. & TENENBAUM, A. 1992 Adaptive self-organisation during growth of bacterial colonies. *Physica A* **187**, 378–424.

BUNGER, A. P. & CRUDEN, A. R. 2011 Modelling the growth of laccoliths and large mafic sills: Roll of magma body forces. *J. Geophys. Res.* **116**, B02203.

CARVALHO, M. S. & SCRIVEN, L. E. 1997 Deformable roll coating flows: steady state and linear perturbation analysis. *J. Fluid Mech.* **339**, 143–172.

CARVALHO, M. S. & SCRIVEN, L. E. 1999 Three-dimensional stability analysis of free surface flows: Application to forward deformable roll coating. *J. Comp. Phys.* **151**, 534–562.

CHEN, J. D. 1989 Growth of radial viscous fingers in a Hele-Shaw cell. *J. Fluid Mech.* **201**, 223–242.

CHONG, Y. H., GASKELL, P. H. & KAPUR, N. 2007 Coating with deformable rolls: An experimental investigation of ribbing instability. *Chem. Eng. Sci.* **62**, 4138–4145.

CINAR, Y., RIAZ, A. & TCHELEPI, H. A. 2009 Experimental study of CO_2 injection into saline formations. *Soc. Pet. Eng. J.* **14**, 589–594.

CLANET, C. & SEARBY, G. 1998 First experimental study of the Darrieus-Landau instability. *Phys. Rev. Lett.* **80** (17), 3867–3870.

DEMMEL, J. W., EISENSTAT, S. C., GILBERT, J. R., LI, X. S. & LIU, J. W. H. 1999 A supernodal approach to sparse partial pivoting. *SIAM J. Matrix Anal. A.* **20** (3), 720–755.

DIAS, E. O., ALVAREZ-LACALLE, E., CARVALHO, M. S. & MIRANDA, J. A. 2012 Minimization of viscous fluid fingering: a variational scheme for optimal flow rates. *Phys. Rev. Lett.* **109**, 144502.

DIAS, E. O. & MIRANDA, J. A. 2010 Control of radial fingering patterns: A weakly nonlinear approach. *Phys. Rev. E* **81**, 016312.

FAST, P., KONDIC, L., SHELLEY, M. J. & PALFFY-MUHORAY, P. 2001 Pattern formation in non-Newtonian Hele-Shaw flow. *Phys. Fluids* **13**, 1191–1212.

GADÊLHA, H. & MIRANDA, J. A. 2009 Effects of normal viscous stresses on radial viscous fingering. *Phys. Rev. E* **79**, 066312.

GROTBERG, J. B. & JENSEN, O. E. 2004 Biofluid mechanics in flexible tubes. *Annu. Rev. Fluid Mech.* **36**, 121–147.

HEAP, A. & JUEL, A. 2008 Anomalous bubble propagation in elastic tubes. *Phys. Fluids* **20**, 081702.

HEIL, M. & HAZEL, A. 2011 Fluid-structure interaction in internal physiological flows. *Ann. Rev. Fluid Mech.* **43**, 141–162.

HEIL, M. & HAZEL, A. L. 2006 `oomph-lib` – an object-oriented multi-physics finite-element library. In *Fluid-Structure Interaction* (ed. M. Schäfer & H.-J. Bungartz), pp. 19–49. Springer, `oomph-lib` is available as open-source software at `http://www.oomph-lib.org`.

HOMSY, G. M. 1987 Viscous fingering in porous medium. *Ann. Rev. Fluid Mech.* **19**, 271–311.

HOSOI, A. E. & MAHADEVAN, L. 2004 Peeling, healing, and bursting in a lubricated elastic sheet. *Phys. Rev. Lett.* **93**, 137802.

AL HOUSSEINY, T. T., TSAI, P. A. & STONE, H. A. 2012 Control of interfacial instabilities using flow geometry. *Nat. Phys* **8**, 747–750.

HULL, D. 1999 *Fractology*. Cambridge University Press.

JENSEN, O. E., HORSBURGH, M.K., HALPERN, D. & III, D. P. GAVER 2002 The steady propagation of a bubble in a flexible-walled channel: Asymptotic and computational models. *Phys. Fluids* **14**, 443–457.

JUEL, A. 2012 Flattened fingers. *Nat. Phys.* **8**, 706–707.

KIM, H., FUNADA, T., JOSEPH, D. D. & HOMSY, G. M. 2009 Viscous potential flow analysis of radial fingering in a Hele-Shaw cell. *Phys. Fluids* **21**, 074106.

KONDIC, L., SHELLEY, M. J. & PALFFY-MUHORAY, P. 1998 Non-Newtonian Hele-Shaw flow and the Saffman-Taylor instability. *Phys. Rev. Lett.* **80**, 1433–1436.

LANDAU, L. D. & LIFSHITZ, E. M. 1970 *Theory of elasticity, 2d ed.*. Pergamon Press.

LI, S., LOWENGRUB, J. S., FONTANA, J. & PALFFY-MUHORAY, P. 2009 Control of viscous fingering patterns in a radial Hele-Shaw cell. *Phys. Rev. Lett.* **102**, 174501.

LISTER, J. R., PENG, G. G. & NEUFELD, J. A. 2013 Spread of a viscous fluid beneath an elastic sheet. *Submitted to Phys. Rev. Lett.* .

McEwan, A. D. & Taylor, G. I. 1966 The peeling of a flexible strip attached by a viscous adhesive. *J. Fluid Mech.* **26**, 1–15.

Michaut, C. 2011 Dynamics of magmatic intrusions in the upper crust: Theory and applications to laccoliths on Earth and the Moon. *J. Geophys. Res.* **116**, B05205.

Miranda, J. A. & Widom, M. 1998 Radial fingering in a HeleShaw cell: a weakly nonlinear analysis. *Physica D* **120**, 315–328.

Mullins, W. W. & Sekerka, R. F. 1964 Stability of a planar interface during solidification of a dilute binary alloy. *J. Appl. Phys.* **35**, 444–451.

Orr Jr., F. M. & Taber, J. J. 1984 Use of carbon dioxide in enhanced oil recovery. *Science* **224**, 563–569.

Paterson, L. 1981 Radial fingering in a Hele-Shaw cell. *J. Fluid Mech.* **113**, 513–529.

Pihler-Puzović, D., Illien, P., Heil, M. & Juel, A. 2012 Suppression of complex fingerlike patterns at the interface between air and a viscous fluid by elastic membranes. *Phys. Rev. Lett.* **108**, 074502.

Reinelt, D. A. 1987 Interface conditions for two-phase displacement in Hele-Shaw cells. *J. Fluid Mech.* **183**, 219–244.

Reinelt, D. A. 1995 The primary and inverse instabilities of directional viscous fingering. *J. Fluid Mech.* **285**, 303–327.

Reynolds, O. 1886 On the theory of lubrication and its application to Beauchamp Tower's experiment. *Phil. Trans. Roy. Soc. Lond. A* **117**, 157–234.

Saffman, P. G. & Taylor, G. I. 1958 The penetration of a fluid into a porous medium or Hele-Shaw cell containing a more viscous liquid. *Proc. Roy. Soc. Lond. A* **245**, 312–329.

Shewchuk, J. R. 1996 Engineering a 2D quality mesh generator and delaunay triangulator. In *Applied Computational Geometry: Towards Geometric Engineering Vol. 1148 of Lecture Notes in Computer Science* (ed. M. C. Lin & D. Manocha), pp. 203–222. Springer-Verlag, Berlin (From the First ACM Workshop on Applied Computational Geometry).

Taylor, G. I. 1963 Cavitation of a viscous fluid in narrow passages. *J. Fluid Mech.* **16**, 595–619.

Thomé, T., Rabaud, M., Hakim, V. & Couder, Y. 1989 The Saffman-Taylor instability: From the linear to the circular geometry. *Phys. Fluids A* **1**, 224–240.

Zienkiewicz, O. C. & Zhu, J. Z. 1992 The superconvergent patch recovery and a posteriori error estimates. part 1: The recovery technique. *Int. J. Numer. Meth. Eng.* **33** (7).